Icarus 261 (2015) 91–99

Contents lists available at ScienceDirect

Icarus

journal homepage: www.journals.elsevier.com/icarus

Comment

Investigating the onset of multi-ring impact basin formation

Ross W.K. Potter *

Department of Earth, Environmental and Planetary Sciences, Brown University, Providence, RI 02912, USA
NASA Solar System Exploration Research Virtual Institute

ARTICLE INFO

Article history:
Received 16 April 2015
Revised 6 August 2015
Accepted 7 August 2015
Available online 13 August 2015

Keywords:
Impact processes
Cratering
Moon, surface
Moon, interior
Tectonics

ABSTRACT

Multi-ring basins represent some of the largest, oldest, rarest and, therefore, least understood impact crater structures. Various theories have been put forward to explain their formation; there is currently, however, no consensus. Here, numerical modeling is used to investigate the onset of multi-ring basin formation on the Moon using two thermal profiles suitable for the lunar basin-forming epoch. Various multi-ring basin formation hypotheses are discussed, compared, and evaluated against target deformation and strain distribution in the models, as well as geological and geophysical observations. The mechanism that most closely resembles the numerical models in terms of basin formation and structure, as well as observations, appears to be the ring tectonic theory, whereby ring formation is dependent on transient cavities penetrating entirely through the Moon's lithosphere into the asthenosphere below. The numerical models suggest that all lunar basins larger than Schrödinger (320 km diameter) should be capable of forming multiple rings, as their transient cavities penetrate into the asthenosphere for both thermal profiles. Additionally, the models demonstrate that the target's thermal profile starts to influence basin formation and structure when impact energy exceeds that of the Schrödinger event.

1. Introduction

Impact basins are the largest and oldest form of impact crater structure. Recognized initially on the Moon (Baldwin, 1949, 1963; Hartmann and Kuiper, 1962) they are defined as impact structures consisting of two or more topographic rings. Peak-ring basins possess two topographic rings: the peak-ring – a circular-shaped, mountainous region around the basin center, and a crater rim – usually a topographic-high structure with terrace and slump structures inside of it. On the Moon, peak-ring basins (e.g., 320 km diameter Schrödinger) occur at diameters above ~220 km (Baker et al., 2011). As basins increase in size, one (or more) additional topographic rings are present (e.g., 930 km diameter Orientale, first noted by Hartmann and Kuiper, 1962). These additional rings are also generally circular-shaped mountainous regions. Basins with these additional rings are known as multi-ring basins.

Multi-ring basins are the rarest and, therefore, the least understood crater type. Various theories have been put forward to explain their formation and structure: volcanic modification (Hartmann and Yale, 1968), the hydrodynamic/tsunami model (van Dorn, 1968; Baldwin, 1974; Murray, 1980), megaterracing (Head, 1974), nested craters (Hodges and Wilhelms, 1978), ring tectonics (Melosh and McKinnon, 1978; Melosh, 1989), and the nested melt cavity (Head, 2010). Observational analysis of scores of multi-ring basins on the Moon, Mars, and Mercury (Pike and Spudis, 1987) suggests basin rings are evenly spaced at a ratio of $\sqrt{2}$ (see also Hartmann and Kuiper, 1962; Baldwin, 1963). Some basins have been observed to possess half a dozen, or more, ring structures (Pike and Spudis, 1987). Evidence for a number of these rings is, however, scant and based solely on isolated massifs located at the appropriate $\sqrt{2}$ distance; re-analysis of basins using newer data sets (e.g., Lunar Orbiter Laser Altimeter: Baker et al., 2011) has, in fact, refuted a number of previous ring assignments. The validity of this geometric spacing, therefore, remains questionable, adding further uncertainty to the formation and structure of multi-ring basins. Nevertheless, the number, structure and features of basin rings are inherently tied to the basin-forming process, with many of the above theories suggesting rings are associated with some kind of impact-induced faulting. A consensus on the processes responsible for multi-ring basin formation, though, remains elusive.

Interestingly, the very largest basins, such as South Pole-Aitken on the Moon; Caloris on Mercury; and Hellas on Mars, appear to possess no more than two rings. These basins may have originally possessed multiple rings, but these could have been eroded, relaxed or buried (i.e., by volcanic flows) over time, especially considering their age. South Pole-Aitken, for example, may be 4.3 Ga (Morbidelli et al., 2012).

In this work, the transition between peak-ring basins and multi-ring basins is investigated through numerical modeling of lunar basin-forming impacts. Various hypotheses for multi-ring basin formation are discussed, compared, and evaluated against the numerical model results, as well as observational evidence. On analysis, the ring tectonic theory for multi-ring basin formation (Melosh and McKinnon, 1978; Melosh, 1989) appears the closest approximation when comparing to the numerical model results and geological and geophysical data (though other theories cannot be entirely dismissed). This work also suggests that (i) the pre-impact target thermal profile only starts to affect lunar basin formation and structure for events larger than Schrödinger and, partly as a consequence of this, (ii) all lunar basins greater than Schrödinger should have been capable of forming multiple rings.

2. Methods

The two-dimensional iSALE shock physics code (Collins et al., 2004; Wünnemann et al., 2006), an extension of the SALE hydrocode (Amsden et al.,

* Address: Department of Earth, Environmental and Planetary Sciences, Brown University, Box 1846, Providence, RI 02912, USA.
E-mail address: ross_potter@brown.edu.

http://dx.doi.org/10.1016/j.icarus.2015.08.009
0019-1035/

1980), was used to simulate lunar basin-forming impacts. iSALE has previously been used to study other large-scale impacts such as Chicxulub on Earth (Collins et al., 2008) and South Pole-Aitken on the Moon (Potter et al., 2012a). The two-dimensionality of the code limited impacts to 90° (vertically downward). Though vertical impacts are highly unlikely, they provide a reasonable proxy for oblique (~45°) impacts (for example, experiments and modeling demonstrate craters remain circular in shape down to impact angles of 15–20°: Gault and Wedekind, 1978; Davison et al., 2011) and should produce the correct azimuthally-averaged behavior.

Impactor size (20–120 km diameter) and velocity (10–20 km/s) parameter space was chosen to produce impact structures ~300–1000 km in diameter – the approximate size range of impact basins on the Moon (excluding South Pole-Aitken). Resolution was fixed at 20 cells per projectile [impactor] radius (CPPR). This is consistent with spatial resolutions applied in other basin-scale numerical modeling studies (e.g., Ivanov, 2005; Ivanov et al., 2010; Potter et al., 2013a) whereby large-scale features, important to this type of modeling, are largely insensitive to resolutions of ~10–40 CPPR. Additionally, 20 CPPR provides a reasonable trade-off between resolution and computation time (as impactor size increased, cell size and computation time, decreased).

The axisymmetric halfspace target was divided into crustal and mantle layers. Crustal thicknesses of 60 km and 40 km, based on gravity-derived lunar crustal thickness data (Wieczorek and Phillips, 1999; Hikida and Wieczorek, 2007; Wieczorek et al., 2013), were used. A Tillotson equation of state for gabbroic anorthosite (Ahrens and O'Keefe, 1977; Potter et al., 2012b) and a semi-analytical equation of state (ANEOS) for dunite (Benz et al., 1989) were used to represent the crust and mantle, respectively. As a suitable proxy for asteroidal material (Pierazzo et al., 1997), the dunite ANEOS was also used to represent the impactor. The strength and thermal properties of these materials were taken from gabbro (Azmon, 1967; Stesky et al., 1974; Shimada et al., 1983) and dunite (Shimada et al., 1983; Ismail and Murrell, 1990) laboratory experiment data; curves for mantle melt temperature as a function of pressure for dunite were taken from Davison et al. (2010). The strength and damage models used here are described in Collins et al. (2004) and Ivanov et al. (2010), respectively. For a complete list of crustal and mantle parameters used, please see Potter et al. (2013a). Gravitational acceleration was a constant 1.62 m/s^2.

As basin size increases, the curvature of the target body will begin to influence aspects of basin formation (i.e., ejecta distribution). Because of this, Ivanov et al. (2010) and Potter et al. (2012a) both employed full spherical targets when modeling lunar impact basins >1000 km in diameter. Potter et al. (2015), however, demonstrated that for lunar basin-forming impacts up to ~1000 km in diameter – the approximate limit of basins in this study – halfspace targets are a suitable set up choice.

The majority of impact basins across the Solar System may have formed ~4 Ga, during what has been termed the Late Heavy Bombardment. Planetary bodies ~4 Ga are likely to have been far hotter than they are today. Consequently, suitable thermal profiles estimating internal planetary conditions during this bombardment are required (e.g., Ivanov et al., 2010). In this work, the lunar thermal evolution models of Spohn et al. (2001) were used to estimate lunar thermal conditions ~4 Ga. Two thermal profiles (TP1 and TP2) were investigated. These are the same as those used in Potter et al. (2012b) and comparable to those of Ivanov et al. (2010) and the ~3.5–4 Ga lunar thermal evolution profiles of Laneuville et al. (2013) used in the basin modeling work of Miljković et al. (2013). Both of the profiles used here have similar crustal temperature gradients (10 K/km), however temperatures in the upper mantle are at the solidus in TP1 but remain below the solidus in TP2 (Fig. 1a). The thermal profile also directly affects target strength as geological materials lose strength as their temperature increases; notably all shear strength is lost upon melting at low strain rates (e.g., Jaeger and Cook, 1969). In iSALE, this relation is approximated by the equation (after Ohnaka, 1995)

$$Y_t/Y = \tanh[\xi(T_m/T) - 1] \quad (1)$$

where Y_t is the material's thermally-weakened yield strength, Y is material strength at low temperature, T is the ambient temperature, and ξ is a material constant. T_m is the solidus (at pressure P), which is calculated using the Simon approximation (Poirier, 1991)

$$T_m = T_0(P/a + 1)^{1/c} \quad (2)$$

where T_0 is the solidus at normal pressure, and a and c are material constants found by fits to experimentally-derived peridotite melting data (McKenzie and Bickle, 1988). As ambient temperature approaches the solidus, the bracket on the right hand side of Eq. (1) tends to zero, thus material strength disappears at the solidus (Fig. 1b). At greater depths in the mantle, strength starts to slowly increase.

During the high strain rates of an impact, however, super solidus material will maintain some resistance to deformation as it will contain a mixture of melt and hot and cold clasts. This may be rate-dependent, pressure dependent, or both. A rate-dependent strength was calculated by

$$Y_{eff} = (1 - \tanh[\xi(T_m/T) - 1])\eta_{eff}\dot{\epsilon}_p \quad (3)$$

where η_{eff} is the partial melt (effective) viscosity of the super solidus material and $\dot{\epsilon}_p$ is the second invariant of the plastic strain rate (see Potter, 2012). Eq. (1) was

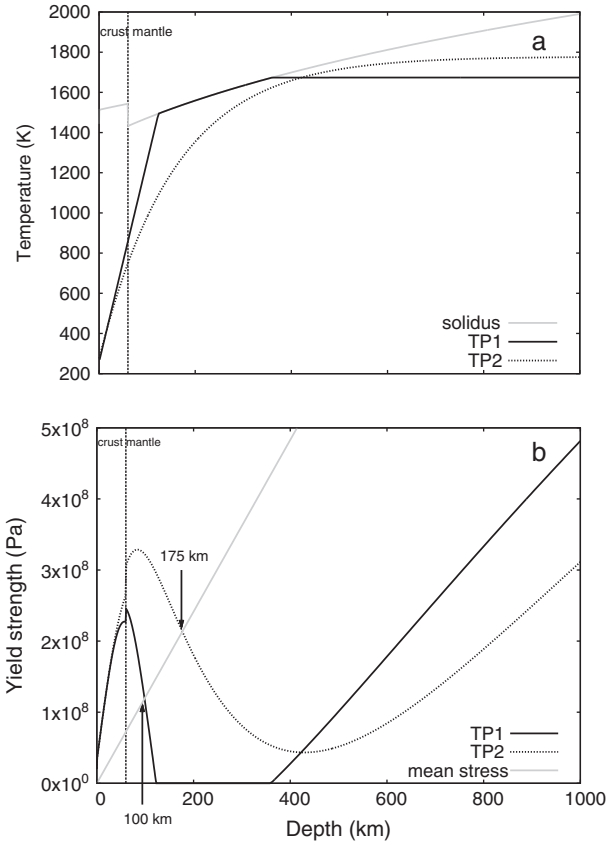

Fig. 1. (a) Temperature-depth profiles for thermal profiles (TP) 1 and 2. (b) Yield strength against depth for TP1 and TP2. The mean stress, 1/4(ρgz), is shown by the solid gray line. Intersection of this line with the target yield strength is estimated as the base of the lithosphere.

modified by using the higher of Y_t and Y_{eff}. This form ensures a smooth transition from a rate-independent strength at low temperature (Y_t) to a rate-dependent strength above the solidus (Y_{eff}). A partial melt viscosity of 10^{10} Pa s (Potter, 2012) was used as this did not greatly affect crater collapse time or the formation of structures similar to those suggested and observed for large (basin)-scale impacts (e.g., Chicxulub crater: Collins et al., 2002, 2008). This partial melt viscosity method has previously been applied in other lunar basin numerical modeling (Potter et al., 2012a,b, 2013a,b). It is, however, a first order approximation as the rheology of partially molten material is likely to have a far greater complexity (Stewart, 2011).

Additionally, acoustic fluidization (Melosh, 1979; Melosh and Ivanov, 1999), a mechanism used to invoke the deep-seated gravitational collapse of transient craters in large-scale impacts, is included in the simulations, via the block model (Melosh and Ivanov, 1999). This also follows the approach of previous lunar basin numerical modeling (Potter et al., 2012b, 2013a,b), whereby acoustic fluidization parameters are based on scaling relations from Wünnemann and Ivanov (2003) and constrained by models that reproduce the Chicxulub crater subsurface structure (Collins et al., 2008).

3. Results

3.1. Basin formation and structure: General observations

Fig. 2 illustrates two lunar basin-forming impacts; the left panels show a multi-ring Orientale basin-sized impact (~930 km diameter) using TP1, a 60 km thick crust, a 50 km diameter impactor and 15 km/s impact velocity; the right panels show a peak-ring Schrödinger basin-sized impact (~320 km diameter) using TP2, a 40 km thick crust, a 25 km diameter impactor and 15 km/s impact velocity.

On impact, the growing transient cavity both excavates (out of the crater) and displaces (beneath the cavity floor) target material. When the cavity reaches its maximum volume, it is defined here to represent the transient crater (Fig. 2a), in line with previous numerical modeling (e.g., Elbeshausen et al., 2009). The impact-induced cavity, however, achieves its maximum depth (not shown here) prior to reaching its maximum volume. Differences between the maximum cavity depth and transient crater depth in the models are not, however, substantial (<10%). The floor of the transient crater continues to rise (while the cavity diameter